# The cosmological bulk flow: consistency with ΛCDM and $z \approx 0$ constraints on $\sigma_8$ and $\gamma$

Adi Nusser[1]

*Physics Department and the Asher Space Science Institute-Technion, Haifa 32000, Israel*

Marc Davis[2]

*Departments of Astronomy & Physics, University of California, Berkeley, CA. 94720*

## ABSTRACT

We derive estimates for the cosmological bulk flow from the SFI++ Tully-Fisher (TF) catalog. For a sphere of radius $40h^{-1}$ Mpc centered on the MW, we derive a bulk flow of $333\pm38$ km s$^{-1}$ towards Galactic $(l,b) = (276^\circ, 14^\circ)$ within a $3^\circ$ $1\sigma$ error. Within a $100h^{-1}$ Mpc we get $257\pm44$ km s$^{-1}$ towards $(l,b) = (279^\circ, 10^\circ)$ within a $6^\circ$ error. These directions are at a $40^\circ$ with the Supergalactic plane, close to the apex of the motion of the Local Group of galaxies after the Virgocentric infall correction. Our findings are consistent with the ΛCDM model with the latest WMAP best fit cosmological parameters. But the bulk flow allows independent constraints. For WMAP inferred Hubble parameter $h = 0.71$ and baryonic mean density parameter $\Omega_b = 0.0449$, the constraint from the bulk flow on the matter density $\Omega_m$, the normalization of the density fluctuations, $\sigma_8$, and the growth index, $\gamma$, can be expressed as $\sigma_8\Omega_m^{\gamma-0.55}(\Omega_m/0.266)^{0.28} = 0.86\pm0.11$ (for $\Omega_m \approx 0.266$). Fixing $\sigma_8 = 0.8$ and $\Omega_m = 0.266$ as favored by WMAP, we get $\gamma = 0.495 \pm 0.096$. The constraint derived here rules out popular DGP models at more than the 99% confidence level. Our results are based on a method termed ASCE (All Space Constrained Estimate) which reconstructs the bulk flow from an all space three dimensional peculiar velocity field constrained to match the TF measurements. At large distances ASCE generates a robust bulk flow from the SFI++ that is insensitive to the assumed prior. For comparison, a standard straightforward maximum likelihood estimate leads to very similar results.

*Subject headings:* Cosmology: large-scale structure of the Universe, dark matter, cosmological parameters

[1]E-mail: adi@physics.technion.ac.il

[2]E-mail: mdavis@berkeley.edu

## 1. Introduction

Cosmological bulk flows are the peculiar velocities of whole spherical regions around us. Bulk flows are usually considered for sufficiently large spheres where linear expressions for the velocity and density power spectra are valid. This greatly facilitates the calculation of expected bulk flows in cosmological models, in contrast to analyzing the full field field which may involve non-linear effects on small scales (Feldman et al. 2010; Abate & Erdoğdu 2009; Zaroubi et al. 2001; Freudling et al. 1999). In linear theory, the bulk flow of a sphere is solely determined by the gravitational pull of only the dipole component of the external mass distribution. Bulk flows are, therefore, an unmistakable indicator of distant large mass concentrations should they exist. The exact expression of the bulk flow, $\mathbf{B}(r)$, of a sphere of radius $r$ is,

$$\mathbf{B}(r) = \frac{3}{4\pi r^3} \int_{x<r} \boldsymbol{v}(\boldsymbol{x}) \mathrm{d}^3 x \ . \tag{1}$$

where $\boldsymbol{v}(\boldsymbol{x})$ is the 3D peculiar velocity field as a function of the comoving coordinate $\boldsymbol{x}$. Beneath this innocuous expression lie a multitude of nuisances. An unbiased estimate of $\mathbf{B}$ requires knowledge of $\boldsymbol{v}$ sampled uniformly overall the volume. However, observational probes of peculiar velocities measurements are available only for a few thousand galaxies with a patchy coverage of the local Universe. Further, peculiar velocity probes such as the TF relation allow us to constrain only the radial component of the peculiar velocities of galaxies.

Recently compiled data on peculiar velocities has triggered renewed interest in the analysis of large scale flows, including the bulk flow (Davis et al. 2011; Lavaux et al. 2010; Erdoğdu et al. 2006). Feldman et al. (2010) report an unusually large bulk flow of $416 \pm 78$ km s$^{-1}$ in a sphere of $100h^{-1}$ Mpc which is at odds with the ΛCDM model with the best fit parameters of the Seven-Year Wilkinson Microwave Anisotropy Probe (WMAP7) (e.g. Jarosik et al. 2010; Larson et al. 2010). Here we provide an alternative estimate of the bulk using a single data set of TF measurements of galaxies, trimmed at faint magnitudes to ensure the linearity of the TF relation. The estimate is based on a method which we term ASCE for All Space Constrained Estimate. The method computes $\mathbf{B}(r)$ using (1) from a three dimensional $\boldsymbol{v}(\boldsymbol{x})$ defined everywhere in a large region of space and constrained to match the TF data. For the analysis below, we use the SFI++ survey of spiral galaxies with I-band Tully-Fisher distances, (Masters et al. 2006; Springob et al. 2007), which builds on the original Spiral Field I-band Survey (Giovanelli et al. 1994, 1995; Haynes et al. 1999) and Spiral Cluster I-band Survey (Giovanelli et al. 1997a,b). We use the published SFI++ magnitudes and velocity widths, and derive our own peculiar velocities, rather than taking the published distances as given. We shall use the *inverse* of the Tully-Fisher (ITF) relationship. The main advantages of ITF methods is that samples selected by magnitude, as most are, will be minimally plagued by Malmquist bias effects when analyzed in the inverse direction (Schechter 1980; Aaronson et al. 1982). We assume that the circular velocity parameter, $\eta \equiv \log(\textit{line width})$, of a galaxy is, up to a random scatter, related to its absolute magnitude, $M$, by means of a linear

*inverse* Tully-Fisher (ITF) relation, i.e.,

$$\eta = sM + \eta_0. \tag{2}$$

The preparation of the data is done following Davis et al. (2011). We include all field, group, and cluster galaxies. Galaxies in groups and clusters are treated as individual objects, though the redshifts for template cluster galaxies are replaced by the systematic redshift of the cluster. Galaxies fainter the an estimated magnitude of -20 were removed from the sample as those showed significant deviations from a linear TF relation. In order to get a cleaner TF sample we select only objects with inclination $i > 45^\circ$ to ease problems with inclination corrections. All this leaves us with a sample of 2859 galaxies with redshifts less than $100h^{-1}$ Mpc. The effective depth of the sample defined as the error weighted mean redshift of galaxies is $\sim 40h^{-1}$ Mpc.

We will refer with ΛCDM7 to the ΛCDM cosmological model with the WMAP7 best fit parameters (Larson et al. 2010) for a flat Universe, i.e. the total mass density parameter $\Omega_m = 0.266$, baryonic density parameter $\Omega_b = 0.0449$, a Hubble constant $h = 0.71$ in units of 100 $\mathrm{km\,s^{-1}Mpc^{-1}}$, a scalar spectral index $n_s = 0.963$, and $\sigma_8 = 0.8$ for the rms of linear density fluctuations in spheres of $8h^{-1}$ Mpc. Throughout the paper, variants of ΛCDM7 with different $\Omega_m$ and $\sigma_8$ will be considered. All other parameters will be fixed at their WMAP7 values.

The outline of the paper is as follows. Details of the ASCE method are described in §2, while the more standard Maximum Likelihood Estimate (MLE) outlined in §3. Tests of the methods using mock catalogues designed to match the SFI++ catalogue are presented in §3. Results for the bulk flows from the SFI++ data are given in §5 with the subsection §5.1 providing a comparison with the ΛCDM models. Finally, §6 discusses the results and some of their cosmological implications.

## 2. The All Space Constrained Estimate (ASCE)

Observations of distance (peculiar velocity) indicators, such as the SFI++ TF survey, are available for only a small fraction of galaxies in the local Universe (out to $\sim 100h^{-1}$ Mpc). The absence of uniformly distributed data prevents a direct application of equation (1). To circumvent this problem, the ASCE method effectively uses (1) to reconstruct the bulk flow from a 3D field $\boldsymbol{v}(\boldsymbol{x})$ which satisfies two conditions: a) at sufficiently large distances from the observed galaxies in the TF data, it has a power spectrum that is dictated by a cosmological model such as the ΛCDM, and b) it has radial peculiar velocities at the positions of the observed galaxies, which are consistent with the TF measurements. The approach is similar to that of constrained realization from noisy data (Hoffman & Ribak 1991; Zaroubi et al. 1995), but it is more general and easier to implement. Assume that the TF catalogue contains $i = 1 \ldots N_{\rm g}$ galaxies with measured redshifts (in $\mathrm{km\,s^{-1}}$), $cz_i$, apparent magnitudes, $m_i$, and line width parameters, $\eta_i$. We write the absolute magnitude of

a galaxy,

$$M_i = M_{0i} + P_i \ , \tag{3}$$

where

$$M_{0i} = m_i + 5\log(cz_i) - 15 \tag{4}$$

and

$$P_i = -5\log(1 - u_i/cz_i) \tag{5}$$

with $u_i$ the radial peculiar velocity of the galaxy. Both $cz_i$ and $u_i$ are defined in the frame of the cosmic microwave background radiation (CMB). Assume that an estimate of the underlying cosmological velocity field, $\boldsymbol{v}(\boldsymbol{x})$, can be written as a linear combination of

$$\boldsymbol{v}(\boldsymbol{x}) = \sum_{\alpha}^{N_{\rm a}} a^\alpha \boldsymbol{v}^\alpha(\boldsymbol{x}) \ , \tag{6}$$

where the $N$ fields, $\boldsymbol{v}^\alpha(\boldsymbol{x})$ $(\alpha = 1 \cdots N_{\rm a})$, are gaussian random velocity fields generated using a cosmologically viable power spectrum. In practice these basis velocity fields will be extracted from a linear cosmological velocity field generated in a very large box using the power spectrum of the ΛCDM model. We then compute $u_i^\alpha$, the radial component of the $\boldsymbol{v}^\alpha$ at the redshift space positions of the observed galaxies, and define the $P-$basis functions, $P_i^\alpha = -5\log(1-u_i^\alpha/cz_i)$ for the observed galaxies only. The model $P$ is then written as

$$P_i^M = \sum_\alpha a^\alpha P_i^\alpha \ . \tag{7}$$

The best fit mode coefficients $a^\alpha$, the slope, $s$, and the zero point $\eta_0$, are found by minimizing the $\chi^2$ statistic

$$\chi^2 = \frac{1}{\sigma_\eta^2} \sum_{i=1}^{N_{\rm g}} \left(sM_{0i} + sP_i^M + \eta_0 - \eta_i\right)^2 + \sum_{\alpha=1}^{N_{\rm a}} (a^\alpha)^2 \ , \tag{8}$$

where $\sigma_\eta^2$ is the *rms* of the intrinsic scatter in $\eta$ about the ITF relation, and $N_{\rm g}$ is the number of galaxies in the sample. The second term of the sum over the squares of $a^\alpha$ is introduced in order to regularize the solution especially in regions of poor data coverage. In the appendix we derive this term from a Bayesian formulation. The solution to the equations $\partial\chi^2/\partial a^\alpha = 0$, $\partial\chi^2/\partial s = 0$ and $\partial\chi^2/\partial\eta_0 = 0$ is straightforward. The coefficients $a^\alpha$ will be used in equation (6) to get $\boldsymbol{v}(\boldsymbol{x})$ everywhere in a region of space large enough to contain the data. For each field $\boldsymbol{v}^\alpha(\boldsymbol{x})$ we compute its corresponding bulk flow, $\mathbf{B}^\alpha(r)$, according to equation (1) and write our ASCE bulk flow as

$$\mathbf{B}_{\rm ASCE}(r) = \sum_\alpha a^\alpha \mathbf{B}^\alpha(r) \ . \tag{9}$$

## 3. The Maximum Likelihood Estimate (MLE)

For comparison we will present estimates of the bulk flow obtained with the standard MLE (Kaiser 1988). This method approximates the bulk flow of a sphere of radius $r$ as the vector $\mathbf{B}_{\rm MLE}$ which renders a minimum in

$$\chi^2 = \frac{1}{\sigma_\eta^2} \sum_{cz_i<r} \left( sM_{0i} + 2.17s\frac{\mathbf{B}\cdot\hat{\boldsymbol{r}}_i}{cz_i} + \eta_0 - \eta_i \right)^2 \tag{10}$$

with respect to the three components of $\mathbf{B}$. The sum is over galaxies within $r$ and $\hat{\boldsymbol{r}}_i$ is unit vector in the direction of galaxy $i$. Further, in this expression we have approximated $P = -5\log(1 - \mathbf{B}\cdot\hat{\boldsymbol{r}}_i/cz_i) \approx 2.17\mathbf{B}\cdot\hat{\boldsymbol{r}}_i/cz_i$.

## 4. Tests

In order to test the performance of ASCE and the MLE reconstructions of the bulk flow from the SFI++ TF data we use 2200 mock catalogs of TF measurements. In each of the catalogues, galaxies with the same positions as in the real SFI++ data are assigned absolute magnitudes, $M_i$, and line width parameters, $\eta_i$, following an artificial ITF relation with slope $s = -0.12$ and intrinsic scatter $\sigma_\eta = 0.057$ (e.g. Davis et al. 2011). The peculiar velocities of galaxies in each mock are taken from a linear gaussian random velocity field in a cubic box of $1454h^{-1}$ Mpc on the side. Each mock is placed randomly in this large box and the peculiar velocity of each galaxy is then obtained by interpolating the velocity field on the position of the galaxy. A gaussian random realizaton of the velocity field is generated for ΛCDM7 using the COSMICS package (Ma & Bertschinger 1995). Further, we work with a parametric form of the power spectrum taken from Eisenstein & Hu (1998) (eqs. 29-31 in their paper)

For ASCE we still need to construct the basis velocity fields $\boldsymbol{v}^\alpha(\boldsymbol{x})$. Here we use $N_{\rm a} = 120$ basis functions, extracted in a similar way to the mocks, but from a completely different random realisation of a velocity field in a very large box. Thanks to the regularization term in (8), the ASCE inferred bulk flow has very little dependence on the actual value of $N_{\rm a}$ as long as it is large enough to capture the main features of the 3D flow: very similar results are obtained with $N_{\rm a} = 50$ and $N_{\rm a} = 120$. Each of these 120 velocity fields $\boldsymbol{v}^\alpha(\boldsymbol{x})$ are further smoothed with a gaussian window of $10h^{-1}$ Mpc in width. The purpose of this small scale smoothing is to filter out low frequency modes which would be over-fitted by the data especially at large distances. This smoothing, however, has very little effect on the bulk flows reconstructed by ASCE. We emphasize that a basis function $\boldsymbol{v}^\alpha(\boldsymbol{x})$ is not only defined at the galaxy positions, but also at any point in a sufficiently large volume (radius $100h^{-1}$ Mpc) which contains all the galaxies used in the analysis. Hence, for each basis function we can measure its corresponding bulk flow, $\mathbf{B}^\alpha(r)$, and once coefficients $a^\alpha$ have been determined

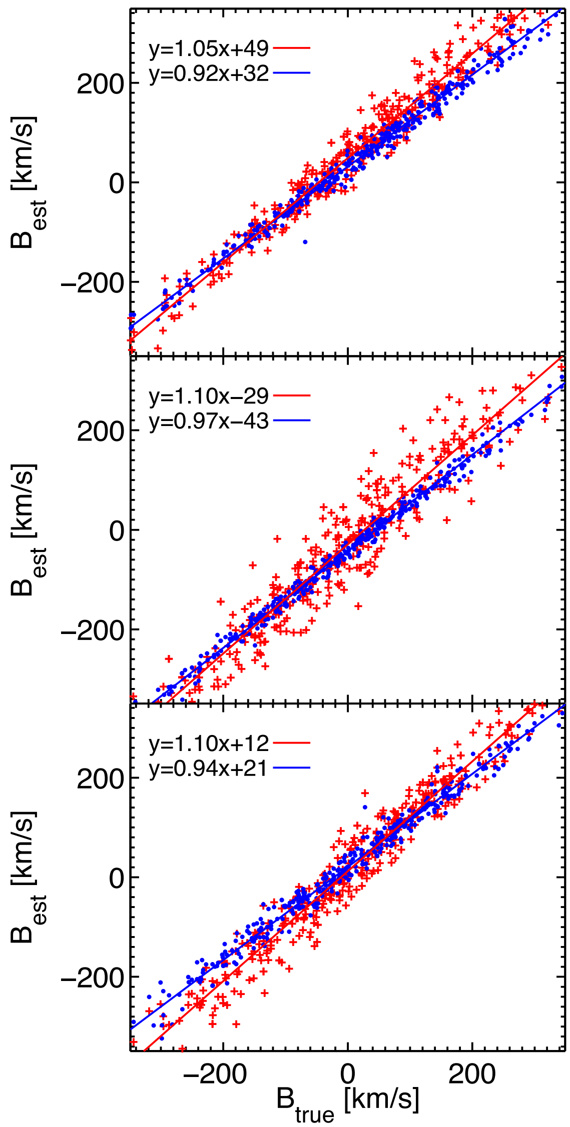


Fig. 1.— Scatter plots of estimated versus true bulk flows in 400 mock catalogues. The **top**, **middle** and **bottom** panels correspond to the Supergalactic $x$, $y$ and $z$ components of the bulk flow. Plotted are bulk flows in a spherical region of $r = 60h^{-1}$ Mpc centered at the origin. Bulk flows from ASCE and MLE are represented as blue dots and red crosses, respectively. The overlaid lines in each panel are linear regressions.

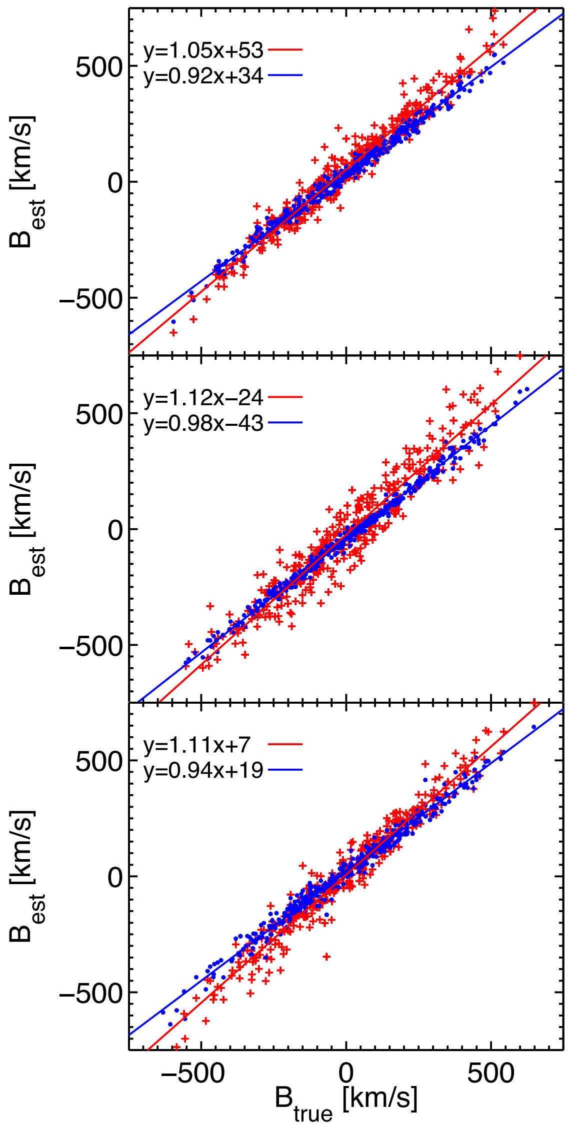


Fig. 2.— The same as the previous figure but where the peculiar velocities in the mocks have been amplified by a factor of 1.5.

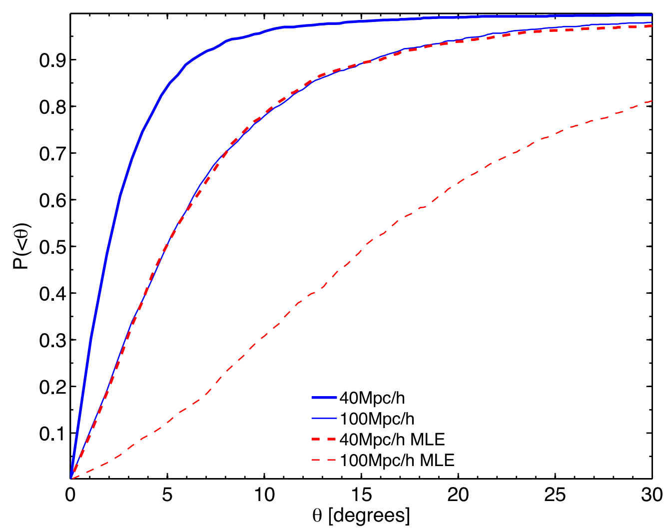


Fig. 3.— The cumulative fraction of mock catalogues with estimated bulks directed within angle smaller than $\theta$ from the direction of the true bulk flow. Blue solid lines and red dashed lines, respectively, correspond to the ASCE and MLE reconstructions. Thick and thin lines, respectively, refer to bulk flows of spheres of radii $40h^{-1}$ Mpc and $100h^{-1}$ Mpc centered on the observer.

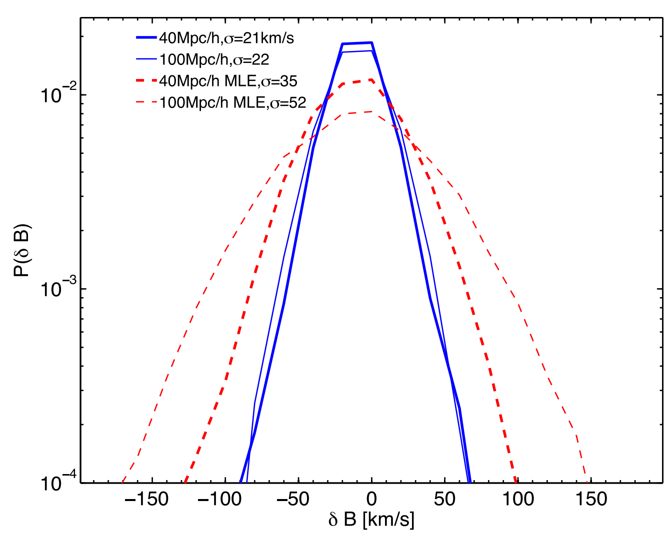


Fig. 4.— The differential distribution functions of the difference between estimated and true respective cartesian components. The notation of the lines is the same as in the previous figure.

from the data by minimization of (8) then the ASCE reconstructed bulk, $\mathbf{B}_{\rm ASCE}(r)$, is readily given by (9).

Figure 1 shows scatter plots of the estimated versus true bulk flows of a spherical region of $60h^{-1}$ Mpc in radius. For clarity, results from only 400 randomly selected mock catalogues are shown. Blue dots and red plus signs correspond to $\mathbf{B}_{\rm MLE}$ and $\mathbf{B}_{\rm ASCE}$, respectively. Because of the anisotropic distribution of the observed galaxies, the methods may not reconstruct the three cartesian components equally well. Hence, $x, y$ and $z$ bulk flow components in Supergalactic coordinates are, respectively, shown in the top, middle and bottom panels. Blue and red lines in each panel are linear regressions of the estimated on true bulk flows. The corresponding mathematical expressions of the regressions are indicated in each panel.

The regularization term in (8) naturally tends to underestimate the coefficients $a^\alpha$ and subsequently the reconstructed bulk flow. However, the agreement between the ASCE reconstructed and the true bulk flows seen in figure (1) clearly demonstrates that the effect is meagre. To further explore the quality of the ASCE and MLE reconstructions and to ascertain that the regularization term does not cause a significant reduction in the amplitude of the bulk flow, we apply ASCE and MLE to the mock data but with true velocities amplified by a factor of 1.5. Everything else, including the regularization term in (8), remained the same. The reconstructed $\mathbf{B}_{\rm ASCE}$ and $\mathbf{B}_{\rm MLE}$ versus true amplified bulk flow are shown in figure (2). Both ASCE and MLE perform well even with this amplification of the bulk flow in the mocks.

In both ASCE and MLE, the slopes of the regression lines plotted in (1) are close, but not equal to unity. The deviation from unity is significant (compared to the scatter of the points) and persists when the regression is done using all the 2200 mock points. This small but statistically significant bias depends on the radius of the sphere for which bulk flow is computed. The bias can easily be calibrated using the mock catalogues. Hereafter, all reconstructed bulk flows, from ASCE and MLE, are corrected for the systematic bias in the mean of the estimated bulk given the mean of the true value. In practice we write the corrected estimate of the bulk flow $\mathbf{B}_{\rm corr}(r)$ from the raw bulk $\mathbf{B}_{\rm raw}(r)$ (directly reconstructed by either ASCE or MLE) as $\mathbf{B}_{\rm corr}(r) = C_1\mathbf{B}_{\rm raw}(r) + C_2$ where $C_1$ is the ratio of the rms values of the true to raw bulk flows and $C_2$ is a constant term which accounts for the offset between the true and raw bulk flows.

In all panels of figure (1), the mock $\mathbf{B}_{\rm ASCE}$ are tightly scattered around their corresponding regression lines. The scatter in $\mathbf{B}_{\rm MLE}$ appears to be more significant. To quantify the scatter between the reconstructed and true bulk flows, we plot, in figure (3), the cumulative fraction, $P<(\theta)$, of mock catalogues for which the angle between estimated and true bulk flows is less than $\theta$. The solid blue and red dashed curves refer to ASCE and MLE, respectively, while thick and thin to bulk flows within $40h^{-1}$ Mpc and $100h^{-1}$ Mpc, also respectively. The curves are computed after employing the correction to the systematic bias as explained above. The performance of ASCE is excellent. For $40h^{-1}$ Mpc, the direction of $\mathbf{B}_{\rm ASCE}$ is recovered within $3^\circ$ for about 68% of the mocks.

For $100h^{-1}$ Mpc this uncertainty increased to 7°. The ASCE method is significantly superior to MLE. The thin blue and thick dashed lines almost overlap, meaning that the performance of ASCE for $100h^{-1}$ Mpc is as as good as that of MLE for $40h^{-1}$ Mpc. For $r = 100h^{-1}$ Mpc, MLE recovers the direction only within 27° for 68% of the mocks.

Figure (4) plots the differential probability distribution function, $P(\delta B)$, where $\delta B$ refers to the difference in all cartesian components between estimated and true bulk flows, from the 2200 mocks. The notation of the lines is the same as in the previous figure and as displayed in the figure. The figure also indicates $\sigma$, the rms value of $\delta B$ for the plotted cases. The low values of $\sigma$ corresponding to ASCE demonstrate its excellent ability at recovering the true bulk. The performance of MLE is good, but less satisfactory.

## 5. Results

The results of the application of the ASCE and MLE methods to recover the bulk flow from the real SFI++ TF catalogue are summarized in figures (5)–(6). The bulk flows are reconstructed for spheres centered on the Milky-Way and of radii from $r = 20h^{-1}$ Mpc to $100h^{-1}$ Mpc in steps of $10h^{-1}$ Mpc. The smallest radius is chosen large enough so that nonlinear effects are not expected to be important (Nusser et al. 1991), facilitating the comparison with cosmological models. The largest radius corresponds to the distance within which the data are used. Figure (5) shows the Galactic $x$ (blue dotted), $y$ (black solid), and $z$ (red dot-dashed) components of $\mathbf{B}_{\rm ASCE}$ (top panel) and $\mathbf{B}_{\rm MLE}$ (bottom) as a function of $r$. The magnitudes of $\mathbf{B}_{\rm ASCE}$ and $\mathbf{B}_{\rm MLE}$ versus radius are plotted, respectively, as the blue circles and plotted in figure (6). The $1\sigma$ errorbars in both figures are based on the 2200 mocks. The component $B_y$ is clearly the most significant. This is just a coincident and has no bearing on the statistical analysis of the results as one can always choose a coordinate system such that the bulk is along a given axis.The solid curve in this figure is the theoretical expectation of ΛCDM7 with but with $\sigma_8 = 0.85$ instead of the default $\sigma_8 = 0.8$. The theoretical curve is computed given the density power spectrum $p_\delta(k, \Omega_m, \Omega_b, h, n_s)$ by

$$\sigma_v^2(r) = \frac{H_0^2 f^2}{2\pi^2} \int {\rm d}k\; p_\delta(k) W^2(kr) \tag{11}$$

where $f = \Omega_m^\gamma$ with a growth index $\gamma \approx 0.55$ for a flat Universe (Linder 2005), and $W = W_{\rm TH}(kr)\exp(-k^2R_s^2/2)$ with $W_{\rm TH}$ is the top-hat window function and the gaussian window takes care of the fact that the basis functions $\boldsymbol{v}^\alpha$ used in ASCE are smoothed with a gaussian window of $R_s = 10h^{-1}$ Mpc in width. The expression (11) is obtained assuming the linear relation $H_0 f\delta = -\nabla\cdot\boldsymbol{v}(\boldsymbol{x})$ between the density contrast, $\delta$, and $\boldsymbol{v}(\boldsymbol{x})$ Peebles (1980).

The MLE and ASCEreconstructed bulks are similar especially at large distances $r > 40h^{-1}$ Mpc. This is because, the data covers space more isotropically at larger distances. Figure (2) clearly

demonstrates that ASCE will not cause a significant artificial under-estimation of large bulk flows such as reported in Feldman et al. (2010). To further, ascertain that our ASCE derived bulk flow is robust, the blue circles in figure (7) the amplitude of the ASCE bulk flow reconstructed using basis functions generated from a ΛCDM7 power spectrum but with a scalar index $n = 0.75$ and $\sigma_8 = 1$. The results are very similar to the ASCE bulk flow shown in figure (6) despite the significantly enhanced large scale power. The agreement is particularly striking at large distances.

### 5.1. Comparison with cosmological models

Figure (6) indicates that the estimated bulk flows are consistent with the theoretical expectations. But the errors are strongly correlated and a proper statistical analysis must take into account the covariance of the errors. Our large number (2200) of mock catalogues allows a robust determination of the error covariance function between the bulk flow estimates at different radii. Since ASCE is significantly superior to MLE, we restrict the comparison with models to ASCE reconstruction. We use all components of $\mathbf{B}_{\rm ASCE}$ estimated at 8 values of $r$ ranging from $r = 30h^{-1}$ Mpc to $100h^{-1}$ Mpc in steps of $10h^{-1}$ Mpc. The reason for not considering smaller radii is that the bulk is most robustly constrained independent of the assumed basis functions at $r > 30h^{-1}$ Mpc. We denote the set of ASCE reconstructed cartesian components at these 8 values of $r$ by $\mathcal{B}_{\rm t}$ and the corresponding underlying true quantities by $\mathcal{B}_t$. We write the probability for observing the set $\mathcal{B}_{\rm o}$ as

$$P(\mathcal{B}_{\rm o}) = \int {\rm d}\mathcal{B}_{\rm t} P(\mathcal{B}_{\rm o}|\mathcal{B}_{\rm t}) P(\mathcal{B}_{\rm t}) \tag{12}$$

where the probability $P(\mathcal{B}_{\rm t})$ for the underlying $\mathcal{B}_{\rm t}$ is computed within the framework of a cosmological model. Here, we adopt the ΛCDM model. For gaussian velocity fields, the calculation of $P(\mathcal{B}_{\rm t})$ is easily done by integrating standard analytic expressions involving the power spectrum. We assume that the probability $P(\mathcal{B}_{\rm o}|\mathcal{B}_{\rm t})$ for $\mathcal{B}_{\rm o}$ given $\mathcal{B}_{\rm t}$ is gaussian with error covariance matrix computed from the 2200 mocks. Under these assumptions, the expression (12) yields

$$P(\mathcal{B}_{\rm o}) = \frac{1}{\sqrt{(2\pi)^d |\Sigma|}} \exp\left(-\frac{1}{2}\mathcal{B}_{\rm o}^T \Sigma^{-1} \mathcal{B}_{\rm o}\right) , \tag{13}$$

where $d$ is the number of elements in $\mathcal{B}_{\rm o}$, i.e. $d = 24 = 8 \times 3$; for 8 values of $r$ and 3 cartesian components. The $d \times d$ covariance matrix $\Sigma = \Sigma_{\rm o} + \Sigma_{\rm t}$, where $\Sigma_{\rm o}$ is the covariance of the errors on $\mathcal{B}_{\rm o}$ and $\Sigma_{\rm t}$ describes the covariance of the underlying quantities $\mathcal{B}_{\rm t}$. The dependence on the cosmological models comes through $\Sigma_{\rm t}$.

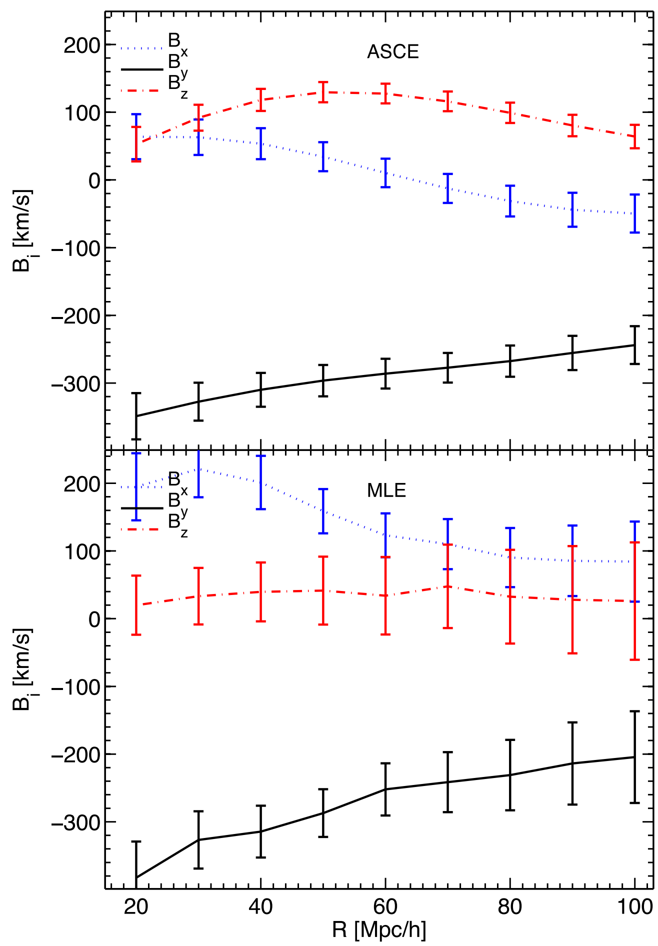


Fig. 5.— The three Galactic cartesian components of the bulk flow as a function of radius. **Top** and **bottom** panels correspond to ASCE and MLE estimation, respectively.

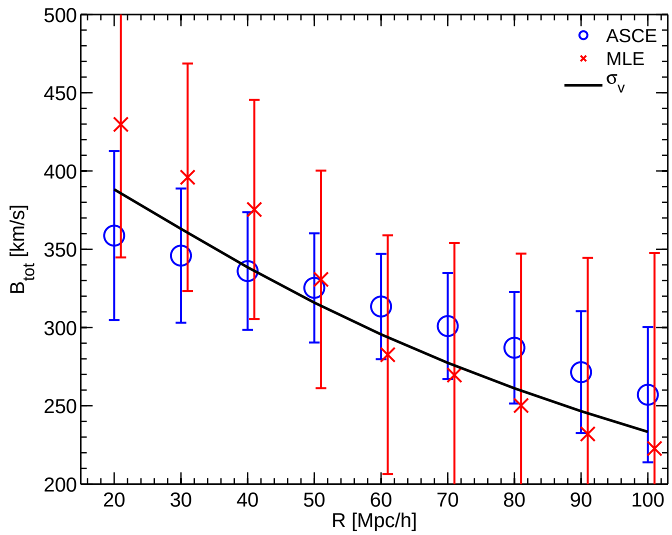


Fig. 6.— The amplitude of the bulk as a function of distance for ASCE and MLE as indicated in the figure. The solid curve shows the rms value of the bulk flow as expected in a flat Universe $\Lambda$CDM model with $\Omega_m = 0.266$, $h = 0.71$ and $\sigma_8 = 0.85$.

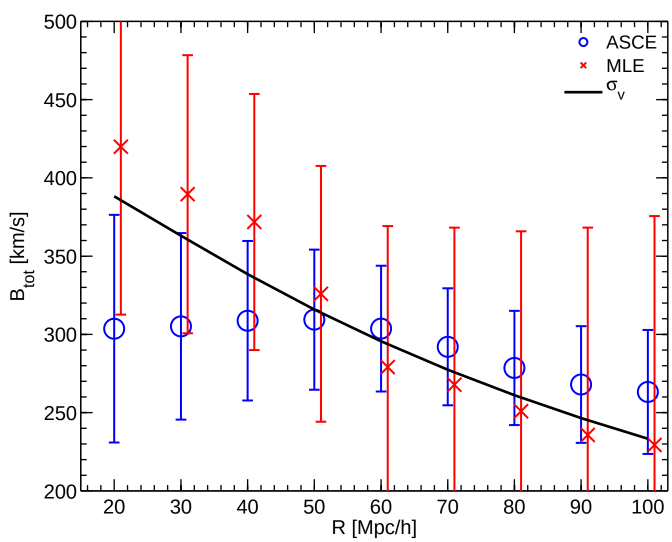


Fig. 7.— The same as the previous figure with ASCE basis functions generated using a $\Lambda$CDM7 power spectrum but with scalar index $n = 0.75$ and $\sigma_8 = 1$, which has more power on large scales compared to our standard choice $n = 0.963$.

### 5.2. Consistency with ΛCDM7

We begin by assessing how well ΛCDM7 is consistent with the data. To do that we generated $10^7$ sets, $\mathcal{B}_{\rm rnd}$, each containing $d = 18$ numbers selected at random from a gaussian distribution given by (13) computed with $\Sigma_{\rm t}$ for ΛCDM7. For each of those $10^7$ sets of $\mathcal{B}_{\rm rnd}$ we compute the corresponding $P(\mathcal{B}_{\rm rnd})$ using (13) and tabulate the negative of the log of the probability, $nlP_{\rm rnd} = -\ln P(\mathcal{B}_{\rm rnd})$. We also compute $nlP_{\rm o} = -\ln P(\mathcal{B}_{\rm o})$ for the observed $\mathcal{B}_{\rm o}$ also using ΛCDM7. We find that only 26% of the $10^7$ values of $nlP_{\rm rnd}$ exceed $nlP_{\rm o}$. Therefore, the ΛCDM7 cannot be rejected by the bulk flow results.

### 5.3. Independent constraints on $\sigma_8$ and $\gamma$

The ΛCDM expected amplitude of the bulk flow depends separately on the cosmological parameters (see equation 11 and the parametric form for the power spectrum in Eisenstein & Hu (1998)). But the most significant dependence is on $\sigma_8$ and $\Omega_m$ and hence we restrict ourselves here to deriving constraints on these two parameters only. We compute $nlP_{\rm o}$ for a grid of values of $\Omega_m$ and $\sigma_8$ used in $\Sigma_{\rm t}$, maintaining all other parameters at their default ΛCDM7 values.

Confidence levels (CLs) on $\Omega_m$ and $\sigma_8$ are obtained by inspecting the contours of $\Delta\chi^2(\Omega_m, \sigma_8) = 2(nlP_{\rm o} - \min(nlP_{\rm o}))$ in the $(\Omega_m, \sigma_8)$ plane. The minimum of $nlP_{\rm o}$ (i.e. $\Delta\chi^2 = 0$ ) is at $(\Omega_m, \sigma_8) = (0.236, 0.88)$, marked by the plus sign in the figure. The ΛCDM7 default values $(\Omega_m, \sigma_8) = (0.266, 0.8)$ are indicated by the circle. The inner and outer contours of $\Delta\chi^2$ shown in figure (8) correspond to 68% and 95% CLs for two degrees or freedom (Press et al. 1992). The ΛCDM7 point is well within the 68% confidence level. The shape of the contours implies the correlation $\sigma_8 \sim \Omega_m^{-0.28}$. This reflects the dependence of the shape of the density power spectrum $p_\delta$ on $\Omega_m$ and from the factor $f(\Omega) \approx \Omega^{0.55}$ (see eq. 11). Only if we neglect the dependence of the shape of $p_\delta$ on $\Omega_m$ we get $\sigma_8 \sim \Omega_m^{0.55}$. It is of interest to inspect the constraints when either of the parameters $\Omega_m$ or $\sigma_8$ is fixed at certain values. Figure (9) shows two curves of $\Delta\chi^2$ versus $\sigma_8$ corresponding to the WMAP7 $\Omega_m = 0.266$ and 0.236 giving a minimum of $\Delta\chi^2$ in the $(\Omega_m, \sigma_8)$ plane as seen in figure (8). Figure (10) plots $\Delta\chi^2$ as a function of $\Omega_m$, for $\sigma_8$ at the WMAP7 value of 0.8 and at 0.88 corresponding to the minimum of $\Delta\chi^2$ in figure (8). In each of the curves in figures (9) and (10), the value of $\Delta\chi^2$ at the minumum of the curve is set to zero. Hence, the $\delta\chi^2 = 1$ and 4 correspond to 68% ($1\sigma$) and 95% ($2\sigma$) CLs, respectively (Press et al. 1992). These curves assume a growth index $\gamma = 0.55$ as is appropriate for a ΛCDM model. Hence figure (9) gives $\sigma_8 = 0.86 \pm 0.11$ ($1\sigma$) for $\Omega_m = 0.266$ and $\gamma = 0.55$. However, we see from (11) that by varying $\gamma$ alone we get the scaling $\sigma_8(\gamma = 0.55) = \sigma_8(\gamma)\Omega_m^{\gamma - 0.55}$. We can use this to set a constraint on $\gamma$ if we adopt $\sigma_8 = 0.8$ and $\Omega_m = 0.266$ (Larson et al. 2010). Demanding that $\sigma_8(\gamma) = 0.8$, the scaling gives $\gamma = 0.496 \pm 0.096$. Figure (11) confirms this result. The figure plots $\Delta\chi^2$ as a function of $\gamma$ for the adopted values

of $\sigma_8$ and $\Omega_m$ as indicated. The left and right arrows mark the values $\gamma = 0.42$ and 11/16. The lower value is expected in $f(R)$ models (e.g. Gannouji et al. 2009) and the highest corresponds to a Dvali-Gabadadze-Porrati (DGP) (Dvali et al. 2000; Wei 2008) flat braneworld cosmology. We could also substitute the scaling with $\gamma$ in the correlation $\sigma_8 \sim \Omega_m^{-0.28}$ obtained from the contour plot to get the constraint $\sigma_8 \Omega_m^{\gamma-0.55}(\Omega_m/0.266)^{0.28} = 0.86 \pm 0.11$ between $\gamma$, $\Omega_m$ and $\sigma_8$.

## 6. Discussion

The analysis presented here uses a trimmed version of the SFI++ in which galaxies fainter than $M = -20$ are removed. This ensures the linearity of the TF relation. Further, to avoid dealing with selection effects imposed on the magnitudes we use the inverse TF relation (see Strauss & Willick (1995) for a thorough review of this issue). Further, to minimize inhomogeneous Malmquist bias (Lynden-Bell et al. 1988), we do not place galaxies at their TF inferred distances, but at their measured redshifts which has significantly smaller observational errors. We also collapse the main known galaxy clusters.

The bulk flows estimated here are remarkably featureless and do not seem to reflect the gravitational effects of any of the individual main nearby clusters. Bulk flow estimates from TF-like relations are traditionally featureless (e.g. Dekel 1994), in contrast to velocity dipoles estimated by from the distribution of galaxies in redshift surveys (e.g. Nusser & Davis 1994). In the analysis here, we have collapsed clusters and therefore, signatures of individual clusters, in our estimated bulk flows, could be smeared out. It is instructive to explore how much we are missing by collapsing clusters and wether signature of infall on clusters of nearby galaxies can actually be clearly seen in SFI++ or similar data. As an illustrative representative case we plot in figure 12 individual peculiar velocities of 54 SFI++ galaxies contained in a cylinder of 6° in radius and of 2600 $\mathrm{km\,s^{-1}}$ centered on the Virgo cluster. The individual distances, $d_{\mathrm{TF}}$ to galaxies are obtained from the observed galaxy deviation from the straight line describing the inverse TF relation as determined by the 54 galaxies. The individual radial peculiar velocities are then given by $V_{\mathrm{TF}} = cz - H_0 d_{\mathrm{TF}}$. Red circles in this figure show $V_{\mathrm{TF}}$ versus $cz$ while the blue plus signs correspond to $V_{\mathrm{TF}}$ versus $d_{\mathrm{TF}}$. The solid line is obtained by statistical regression of $V_{\mathrm{TF}}$ on $cz$, i.e. the red pints. The two straight dashed lines correspond to 95% confidence levels of this regression. The blue points show a pattern that could mistakenly be confused with actual galaxy infall onto Virgo. However, this pattern is entirely due to inhomogeneous Malmquist bias: Galaxies scattered to large estimated $d_{\mathrm{TF}}$ beyond the cluster, will also have a negative inferred $V_{\mathrm{TF}}$. The effect of this Malmquist bias will be more pronounced for more distant clusters which have larger absolute errors on $d_{\mathrm{TF}}$. The red points do not show a clear infall (on Virgo) of galaxies in the immediate vicinity of Virgo. Karachentsev & Nasonova (2010) presents an impressive study of the observed flow of 1792 galaxies near Virgo. Taken into account the inhomogeneous Malmquist bias, it is hard to detect a clear

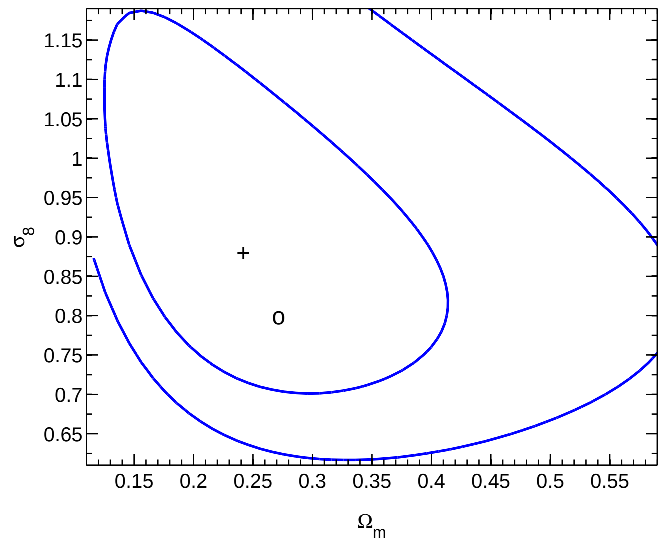


Fig. 8.— Contour plot of the 68% and 95% confidence levels in the $\Omega_m - \sigma_8$ place. The plus sign marks the maximum of the probability distribution function at $(\Omega_m, \sigma_8 = (0.236, 0.88)$, while the circle indicates $(0.266, 0.8)$, corresponding to the best fit WMAP7 values.

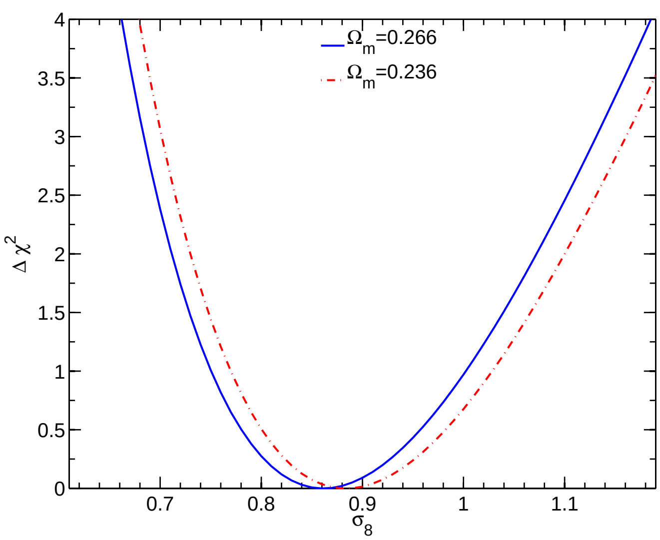


Fig. 9.— Curves of $\Delta\chi^2$ as a function of $\sigma_8$ for $\Omega_m = 0.266$ (blue solid line) and $\Omega_m = 0.236$ (red dot-dashed).

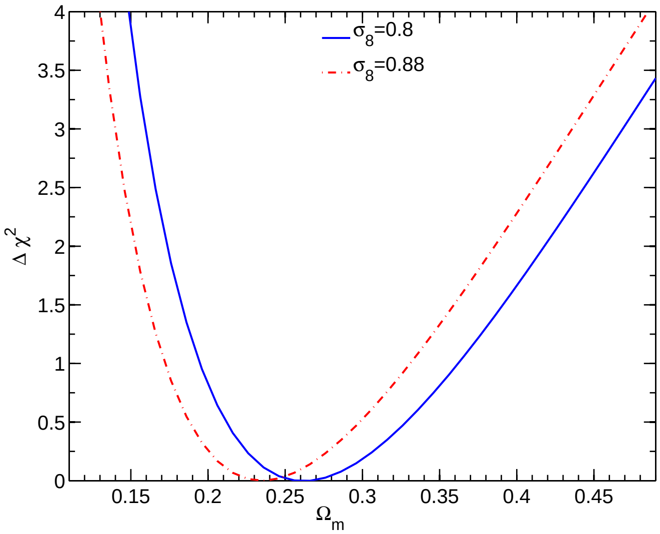


Fig. 10.— Curves of $\Delta\chi^2$ as a function of $\Omega_m$ for $\sigma_8 = 0.8$ (blue solid) and $\sigma_8 = 0.88$ (red dot dashed).

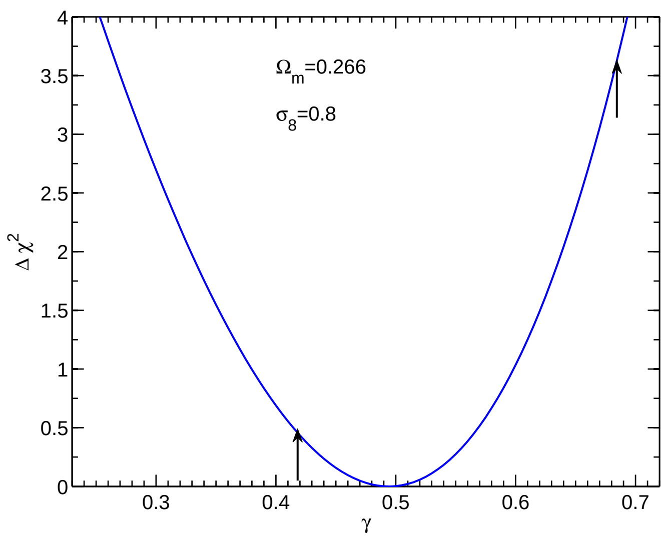


Fig. 11.— Curves of $\Delta\chi^2$ as a function of the growth index $\gamma$ given $\sigma_8 = 0.8$ and $\Omega_m = 0.266$. The left and right arrows, respectively, indicate $\gamma$ values obtained in $f(R)$ and flat DGP models.

infall signature in the near vicinity of Virgo in this study as all (although the focus of their paper is different).

The constraints given in figures (8)–(11) show that the bulk flow alone provides useful additional constraints on the cosmological parameters. To achieve tighter constraints one must investigate the full information in the peculiar velocity measurements. This could be done by analysis of power spectra and correlation functions by maximum likelihood techniques (e.g. Gorski et al. 1989; Jaffe & Kaiser 1995; Zaroubi et al. 1997; Juszkiewicz et al. 2000; Bridle et al. 2001; Abate & Erdoğdu 2009). However, the bulk flow is particularly appealing because of its simplicity and the fact that it is entirely linear for sufficiently large spheres. The constraints from peculiar velocities, including the bulk flow, are unique since they are local at redshifts very close to zero and they directly probe the growth index $\gamma = \frac{\mathrm{dln}f}{\mathrm{d}\Omega_m}$ where $f$ is the linear growth factor (Peebles 1980; Linder 2005). Adopting the WMAP7 cosmological parameters (Larson et al. 2010), we derive a local constraint $\gamma = 0.495 \pm 0.096$. This constraint is completely independent of the biasing relation between galaxies and mass. Further, it is essentially a constraint at $z = 0$. In contrast, the lowest redshift constraint obtained from a study of redshift distortions in the 2dF galaxy redshift survey is at $z \approx 0.15$ (Hawkins et al. 2003). Our constraint significantly improves on previous constraints on $\gamma$ (Dossett et al. 2010; Wei 2008) derived at higher redshifts. This result could help us distinguish between alternative theories for structure formation (e.g. Amendola et al. 2005; Guzzo et al. 2008; Keselman et al. 2010). For $\sigma_8 = 0.8$, the constraint on $\gamma$ disfavors DGP models at $\sim 2\sigma$ level, but it is consistent with $f(R)$ gravity models (e.g. Starobinsky 2007; Gannouji et al. 2009; Wu et al. 2009; Fu et al. 2010). But $\sigma_8$ in these models should be computed self-consistently, assuming the same normalization at the recombination epoch. Based on WMAP7, this implies $\sigma_8 = 0.63$ and 0.855 for DGP and $f(R)$ models, respectively. Adopting these $\sigma_8$ values for these models we get $\gamma = 0.315 \pm 0.091$ and $0.55 \pm 0.098$, respectively, for SGP and $f(r)$ (Cinzia Di Porto, priv. comm). In the DGP model, the expected value for $\gamma$ at $z = 0$ is 0.664 (Wu et al. 2009), which is ruled by our constrain at more than the 3 $\sigma$ level. The $f(R)$ model cannot be ruled out at high confidence level by the constraint derived here.

Our results are in agreement with the analysis of Sandage et al. (2010). Peculiar velocities from supernovae, although very sparse, yield bulk flows that are consistent with WMAP7 (Dai et al. 2011; Colin et al. 2011), as we do. The results are in agreement with the WMAP7. The analysis of Bilicki et al. (2011) of the 2MASS dipole from galaxy fluxes is also in agreement with the WMAP7 LCDM. The direction of the bulk flow is robust and agrees with the direction of the motion of the local group (LG) after correcting for the Virgocentric infall (Sandage et al. 2010). But we disagree strongly with the bulk flows Feldman et al. (2010) who find a significant large bulk flow at $r = 100h^{-1}$ Mpc, using the untrimmed SFI++ survey, other individual data sets and also using a composite catalogue. They also use the TF estimated distances instead of the redshifts in their analysis of the bulk flow, leading to results which are highly susceptible to Malmquist bias. We

have opted to use a single uniformly calibrated catalog, namely the SFI++, excluding faint galaxies which spoil the linearity of the ITF (Davis et al. 2011). We have also refrained from using composite data since minor mis-calibration errors between different catalogs could lead to large artificial flows when these catalogues are combined. Further, we place galaxies at their measured redshifts rather than estimated distances from the TF relation. This greatly suppresses inhomogeneous Malmquist bias which is known to lead to significant spurious signal especial at large distances. We also refrained from using gaussian window so that the bulk flow within a certain radius is completely unaffected by the increasing uncertainties at large distances.

We have seen that the MLE and the ASCE methods give very similar results. Further, the ASCE bulk flow at $r > 30h^{-1}$ Mpc is almost completely independent of the cosmological model used in generating the basis functions. This is clearly demonstrated by the comparison of figures 6 and 7. However, in ASCE even if the results turned out to be sensitive to the assumed model used in generating the basis function, the validity of the model can still be confidently assessed. The reason is that the sensitivity would imply that the data are insufficient for constraining the bulk flow within the framework of the assumed model used in generating the basis function. Fortunately, this ambiguity is irrelevant for the SFI++ used here since the corresponding bulk flow is extremely insensitive to the model used in generating the basis functions.

## 7. Acknowledgments

Special thanks are due to Enzo Branchini for many stimulating discussions. We thank Cinzia Di Porto for providing $\sigma_8$ for the DGP and $f(R)$ models. This work was supported by THE ISRAEL SCIENCE FOUNDATION (grant No.203/09), the German-Israeli Foundation for Research and Development, the Asher Space Research Institute and by the WINNIPEG RESEARCH FUND. MD acknowledges the support provided by the NSF grant AST-0807630.

## REFERENCES

Aaronson, M., Huchra, J., Mould, J., Schechter, P. L., & Tully, R. B. 1982, ApJ, 258, 64

Abate, A., & Erdoğdu, P. 2009, MNRAS, 400, 1541

Amendola, L., Quercellini, C., & Giallongo, E. 2005, MNRAS, 357, 429

Bilicki, M., Chodorowski, M., Mamon, G. A., & Jarrett, T. 2011, ArXiv: 1102.4356

Bridle, S. L., Zehavi, I., Dekel, A., Lahav, O., Hobson, M. P., & Lasenby, A. N. 2001, MNRAS, 321, 333

Colin, J., Mohayaee, R., Sarkar, S., & Shafieloo, A. 2011, MNRAS, 431

Dai, D.-C., Kinney, W. H., & Stojkovic, D. 2011, JCAP, 4, 15

Davis, M., Nusser, A., Masters, K. L., Springob, C., Huchra, J. P., & Lemson, G. 2011, MNRAS, 413, 2906

Dekel, A. 1994, ARAA, 32, 371

Dossett, J., Ishak, M., Moldenhauer, J., Gong, Y., & Wang, A. 2010, JCAP, 4, 22

Dvali, G., Gabadadze, G., & Porrati, M. 2000, Physics Letters B, 485, 208

Eisenstein, D. J., & Hu, W. 1998, ApJ, 496, 605

Erdoğdu, P., et al. 2006, MNRAS, 373, 45

Feldman, H. A., Watkins, R., & Hudson, M. J. 2010, MNRAS, 407, 2328

Freudling, W., et al. 1999, ApJ, 523, 1

Fu, X., Wu, P., & Yu, H. 2010, European Physical Journal C, 68, 271

Gannouji, R., Moraes, B., & Polarski, D. 2009, JCAP, 2, 34

Giovanelli, R., Haynes, M. P., Herter, T., Vogt, N. P., da Costa, L. N., Freudling, W., Salzer, J. J., & Wegner, G. 1997b, AJ, 113, 53

Giovanelli, R., Haynes, M. P., Herter, T., Vogt, N. P., Wegner, G., Salzer, J. J., da Costa, L. N., & Freudling, W. 1997a, AJ, 113, 22

Giovanelli, R., Haynes, M. P., Salzer, J. J., Wegner, G., da Costa, L. N., & Freudling, W. 1994, AJ, 107, 2036

—. 1995, AJ, 110, 1059

Gorski, K. M., Davis, M., Strauss, M. A., White, S. D. M., & Yahil, A. 1989, ApJ, 344, 1

Guzzo, L., Pierleoni, M., Meneux, B., Branchini, E., Le Fèvre, O., Marinoni, C., Garilli, B., & Blaizot, J. e. a. 2008, Nature, 451, 541

Hawkins, E., Maddox, S., Cole, S., Lahav, O., Madgwick, D. S., Norberg, P., Peacock, J. A., & Baldry, I. K. e. a. 2003, MNRAS, 346, 78

Haynes, M. P., Giovanelli, R., Chamaraux, P., da Costa, L. N., Freudling, W., Salzer, J. J., & Wegner, G. 1999, Astrophysical. J, 117, 2039

Hoffman, Y., & Ribak, E. 1991, ApJL, 380, L5

Jaffe, A. H., & Kaiser, N. 1995, ApJ, 455, 26

Jarosik, N., et al. 2010, ArXiv e-prints

Juszkiewicz, R., Ferreira, P. G., Feldman, H. A., Jaffe, A. H., & Davis, M. 2000, Science, 287, 109

Kaiser, N. 1988, MNRAS, 231, 149

Karachentsev, I. D., & Nasonova, O. G. 2010, MNRAS, 405, 1075

Keselman, J. A., Nusser, A., & Peebles, P. J. E. 2010, Physical Review D., 81, 063521

Larson, D., et al. 2010, ArXiv e-prints

Lavaux, G., Tully, R. B., Mohayaee, R., & Colombi, S. 2010, ApJ, 709, 483

Linder, E. V. 2005, Physical Review D., 72, 043529

Lynden-Bell, D., Faber, S. M., Burstein, D., Davies, R. L., Dressler, A., Terlevich, R. J., & Wegner, G. 1988, ApJ, 326, 19

Ma, C., & Bertschinger, E. 1995, ApJ, 455, 7

Masters, K. L., Springob, C. M., Haynes, M. P., & Giovanelli, R. 2006, ApJ, 653, 861

Nusser, A., & Davis, M. 1994, ApJL, 421, L1

Nusser, A., Dekel, A., Bertschinger, E., & Blumenthal, G. R. 1991, ApJ, 379, 6

Peebles, P. J. E. 1980, The large-scale structure of the universe (Princeton University Press)

Press, W. H., Teukolsky, S. A., Vetterling, W. T., & Flannery, B. P. 1992, Numerical recipes in FORTRAN. The art of scientific computing (Cambridge: University Press, —c1992, 2nd ed.)

Sandage, A., Reindl, B., & Tammann, G. A. 2010, ApJ, 714, 1441

Schechter, P. L. 1980, Astronomical Journal, 85, 801

Springob, C. M., Masters, K. L., Haynes, M. P., Giovanelli, R., & Marinoni, C. 2007, ApJ. S, 172, 599

Starobinsky, A. A. 2007, Soviet Journal of Experimental and Theoretical Physics Letters, 86, 157

Strauss, M. A., & Willick, J. A. 1995, Physics Reports, 261, 271

Wei, H. 2008, Physics Letters B, 664, 1

Wu, P., Yu, H., & Fu, X. 2009, JCAP, 6, 19

Zaroubi, S., Bernardi, M., da Costa, L. N., Hoffman, Y., Alonso, M. V., Wegner, G., Willmer, C. N. A., & Pellegrini, P. S. 2001, MNRAS, 326, 375

Zaroubi, S., Hoffman, Y., Fisher, K. B., & Lahav, O. 1995, ApJ, 449, 446

Zaroubi, S., Zehavi, I., Dekel, A., Hoffman, Y., & Kolatt, T. 1997, ApJ, 486, 21

## A. The regularization term

The motivation for the second term on the r.h.s in equation (8) can be found in a a Bayesian statistical formulation. Our model for the three dimensional velocity field defined at any point in space $\boldsymbol{x}$ is given in terms of an expansion, $\boldsymbol{v}^M(\boldsymbol{x}) = \sum_\alpha a^\alpha \boldsymbol{v}^\alpha(\boldsymbol{x})$, over a $N_a$ basis functions $\boldsymbol{v}^\alpha(\boldsymbol{x})$ each corresponding to a realization of a random gaussian field with a cosmologically motivated power spectrum. Given the data, the probability $P(\boldsymbol{v}^M|\mathrm{data})$ for $\boldsymbol{v}^M(\boldsymbol{x})$ is

$$P(\boldsymbol{v}^M|\mathrm{data}) \propto P(\mathrm{data}|\boldsymbol{v}^M)P(\boldsymbol{v}^M)\ , \tag{A1}$$

where $P(\mathrm{data}|\boldsymbol{v}^M)$ is assumed gaussian with $-\ln P(\mathrm{data}|\boldsymbol{v}^M) = \sum_i \left(sM_{0i} + P_i^M + \eta_0 - \eta_i\right)^2/\sigma_\eta^2$ with $P^M$ related to the radial component of $\boldsymbol{v}^M$ by (5). This probability function gives rise to the first term on the r.h.s in equation (8). The *prior* function $P(\boldsymbol{v}^M)$ is the probability for the realization of the particular velocity field model $\boldsymbol{v}^M$ independent of the data. For a gaussian random field

$$-\ln P(\boldsymbol{v}^M) = \sum_{\boldsymbol{x},\boldsymbol{x}',J,J'} v_J^M(\boldsymbol{x})\Xi^{-1}v_{J'}^M(\boldsymbol{x}') \tag{A2}$$

where the indices $J$ and $J'$ refer to the three velocity components and $\Xi(\boldsymbol{x},\boldsymbol{x}',J,J')$ is the velocity correlation function. Substituting the expansion $\boldsymbol{v}^M = \sum_{\alpha=1}^{N_a} a^\alpha \boldsymbol{v}^\alpha$ yields

$$-\ln P(\boldsymbol{v}^M) = \sum_{\alpha,\beta} a^\alpha a^\beta \sum_{\boldsymbol{x},\boldsymbol{x}',J,J'} v_J^\alpha(\boldsymbol{x})\Xi^{-1}v_{J'}^\beta(\boldsymbol{x}')\ . \tag{A3}$$

Since $\boldsymbol{v}^\alpha$ are all space independent fields, the terms with $\alpha \neq \beta$ will be negligibly small. Since all of $\boldsymbol{v}^\alpha$ are generated with the same power spectrum, the term $S = \sum_{\boldsymbol{x},\boldsymbol{x}',J,J'} v_J^\alpha(\boldsymbol{x})\Xi^{-1}v_{J'}^\beta(\boldsymbol{x}')$ will be independent of $\alpha$. Therefore, $-\ln P(\boldsymbol{v}^M) = S\sum_\alpha (a^\alpha)^2$. If the model is also to represent a random realization of the same power spectrum as each of the basis functions $\boldsymbol{v}^\alpha$ then the sum in (A2) must also be equal to $S$. Hence $P(\boldsymbol{v}^M) \propto P(\{a^\alpha\}) \propto \exp(-\sum_\alpha (a^\alpha)^2/2)$ which leads to the second term in (8).

---

This preprint was prepared with the AAS LaTeX macros v5.2.

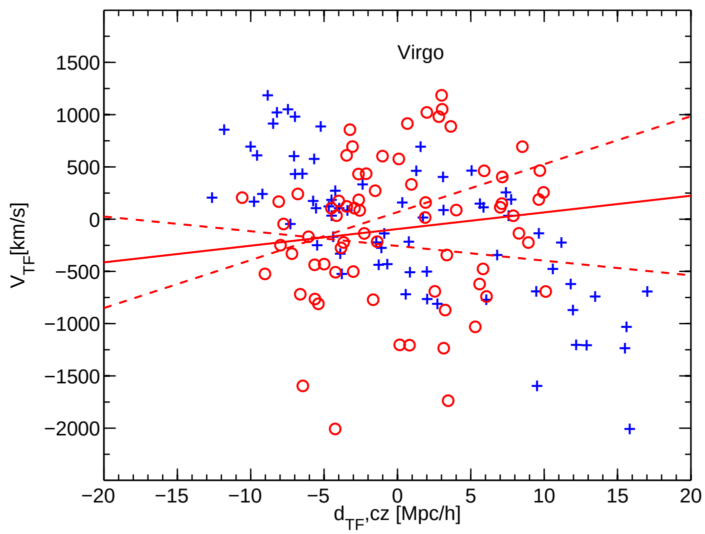


Fig. 12.— Individual peculiar velocities, $V_{\rm TF}$, of galaxies in the line-of-sight to Virgo, plotted against the redshift (red circles) and the estimated distance $d_{\rm TF}$ (blue plus signs). The centroid of these galaxies is at $cz \sim 0$ and $V_{\rm TF} \sim 0$.